# UC San Diego

## UC San Diego Previously Published Works


### Title

Simple shear origin of the cross-faults ruptured in the 2019 Ridgecrest earthquake sequence


### Permalink

https://escholarship.org/uc/item/14b0z3r1



### Journal

Nature Geoscience, 14(7)

### ISSN

1752-0894



### Authors

Fialko, Yuri

Jin, Zeyu



### Publication Date

2021-07-01

### DOI

10.1038/s41561-021-00758-5



### Copyright Information

This work is made available under the terms of a Creative Commons Attribution-NonCommercial License, available at https://creativecommons.org/licenses/by-nc/4.0/

Peer reviewed

eScholarship.org Powered by the California Digital Library
University of California

# Simple shear origin of the cross-faults ruptured in the 2019 Ridgecrest earthquake sequence

Yuri Fialko and Zeyu Jin

*Institute of Geophysics and Planetary Physics, Scripps Institution of Oceanography, University of California San Diego, La Jolla, CA*

*Nature Geoscience, 14*, 513-518, 2021. doi.org/10.1038/s41561-021-00758-5
received 14 July 2020; accepted 14 April 2021; published 03 June 2021

**Observations in tectonically active areas increasingly reveal sets of high-angle conjugate faults ("cross-faults") that apparently contradict theories of faulting based on experimental data. Possible explanations include low in situ coefficient of friction, dominant control of ductile shear zones in the lower crust, and tectonic rotation. Discrimination between these mechanisms has been hindered by uncertainties in the state of stress, deformation history, and fault geometry at seismogenic depths. Here we use a combination of seismic, geodetic, and geologic data to demonstrate that ubiquitous cross-faults in the Ridgecrest (California) area, including those ruptured in the sequence of strong earthquakes in 2019, result from rotation from an initially optimal orientation consistent with experimental data. The inferred rotation pattern can be explained by the geodetically measured velocity field. Our model suggests that the observed asymmetric rotation of faults in the Eastern California Shear Zone can result from simple shear. The same mechanism can be responsible for high-angle conjugate faults observed in other tectonic settings.**

Earthquakes result from unstable slip on faults that are brought to failure by the ambient stress field, however relationships between causal stresses and the consequent seismic ruptures are not well understood. The Mohr-Coulomb-Anderson (MCA) theory predicts that faults should form at an acute angle with respect to the principal compression axis[1,2]. Such an "optimal" angle $\theta_o$ depends solely on the coefficient of friction $\mu$, $\theta_o = \pm 0.5 \arctan(\mu^{-1})$. For typical laboratory values of the coefficient of friction of 0.6-0.8 (the Byerlee's law)[3], the respective angle is $|\theta_o| \sim$25-30 degrees[2,4]. New faults that are produced in the laboratory experiments at a scale of $10^{-2} - 10^{-1}$m, and in nature at a scale of $1 - 10^{3}$m appear to agree with predictions of the MCA theory[5–7]. However, mature (well-slipped) faults are often severely mis-oriented with respect to the present-day stress field[8–11], implying rotation of faults with respect to the principal stress axes, rotation of the principal stress axes, or both, throughout the fault history[12]. Mature faults can operate at high angles with respect to the principal compression axis (and therefore at low resolved shear stress) if they are substantially weaker than the host rocks, owing to either static[13–15] or dynamic[16–19] weakening mechanisms. Many of the proposed weakening mechanisms require extreme localization of slip within a fault zone[20], and such localization may in turn depend on fault maturity[21]. If so, an outstanding question is at which point during a fault evolution may various weakening mechanisms become activated. Alternatively, faults might be weak from their inception[22], implying that either the coefficient of friction is well below the experimentally measured values of 0.6-0.8[3,23], or the pore fluid pressures are well above the hydrostatic. These possibilities can in principle be distinguished by evaluating the orientation of incipient faults with

respect to the principal stress axes. As the latter may not be well known, one can instead use the relative orientation of conjugate faults, under the assumption that the principle compression axis bisects the angle between conjugate planes[2,24]. Unfortunately this approach is not easily applicable to fossil conjugate fault zones because it is not always clear whether different sets of faults were active at the same time. The relationships between active conjugate faults could be studied using seismic focal mechanisms, however uncertainties in the fault plane solutions are typically too large, especially for small to intermediate-size events. Also, the focal mechanisms are essentially indistinguishable in case of high-angle conjugate faults [25]. An optimal data set for a case study would thus involve a sequence of earthquakes that occur on conjugate faults that are relatively immature, yet the earthquakes are large enough not to be treated as point sources. These (rather restrictive) criteria have been met during the 2019 Ridgecrest, California, earthquake sequence, which offered an excellent opportunity to investigate the problem of in situ fault strength.

## Conjugate faulting in the Ridgecrest area

The 2019 Ridgecrest, California, earthquake sequence occurred on a network of northwest (NW) trending right-lateral and northeast (NE) trending left-lateral strike-slip faults[26–28]. The largest events in the sequence were the $M_w$6.4 foreshock and the $M_w$7.1 mainshock (Fig. 1a). The seismic moment release due to the $M_w$7.1 mainshock was dominated by slip on right-lateral faults, and the seismic moment release due to the $M_w$6.4 foreshock was dominated by slip on left-lateral faults[28]. Both the foreshock and the mainshock involved slip on antithetic cross-faults[26,29]. Events comprising the 2019 sequence occurred on immature and largely unmapped faults that were not previously recognized as connected and capable of major earthquakes[30]. The angle between the left- and right-lateral faults ruptured by the $M_w$6.4 foreshock and the $M_w$7.1 mainshock is close to 90 degrees, so that the focal mechanisms based on the moment tensor solutions (see section "Online data" in Supplementary Information) are essentially similar (Fig. 1a). However, because of the earthquake size the sense of motion is unambiguous from the aftershock distribution, as well as surface displacements imaged by field studies and space geodetic observations (Fig. 1b).

We quantified the dihedral angle between faults that produced the foreshock and the mainshock using seismic, geodetic, and geologic data, as well as finite fault models informed by all of the available data (see section "Evaluating the attitude of the 2019 ruptures" in Supplementary Information). The admissible range of angles is 75-100 degrees, with the preferred value of about 85 degrees (Supplementary Fig. 2). As the 2019 Ridgecrest earthquake sequence occurred within a densely instrumented area featuring long-lived seismic and geodetic networks (Supplementary Fig. 3), additional insights can be gained regarding the fault orientation with respect to the principal stress axes. Inversions of focal mechanisms of abundant small local earthquakes indicate an approximately north-south orientation of the maximum horizontal compressive stress $\sigma_{Hmax}$[33]. We used 15-year long time series of displacements from the Plate Boundary Observatory (PBO) network to compute the principal axes of strain rate (see the Methods section and Supplementary Figs. 4 and 6). The axis of the maximum horizontal shortening rate $\dot{\varepsilon}_{Hmax}$ in the neighborhood of the 2019 rupture is oriented $\sim 5^\circ$ east of north (Supplementary Fig. 6). The estimated trajectories of $\sigma_{Hmax}$ and $\dot{\varepsilon}_{Hmax}$ are shown in Fig. 2, along with the precisely relocated background

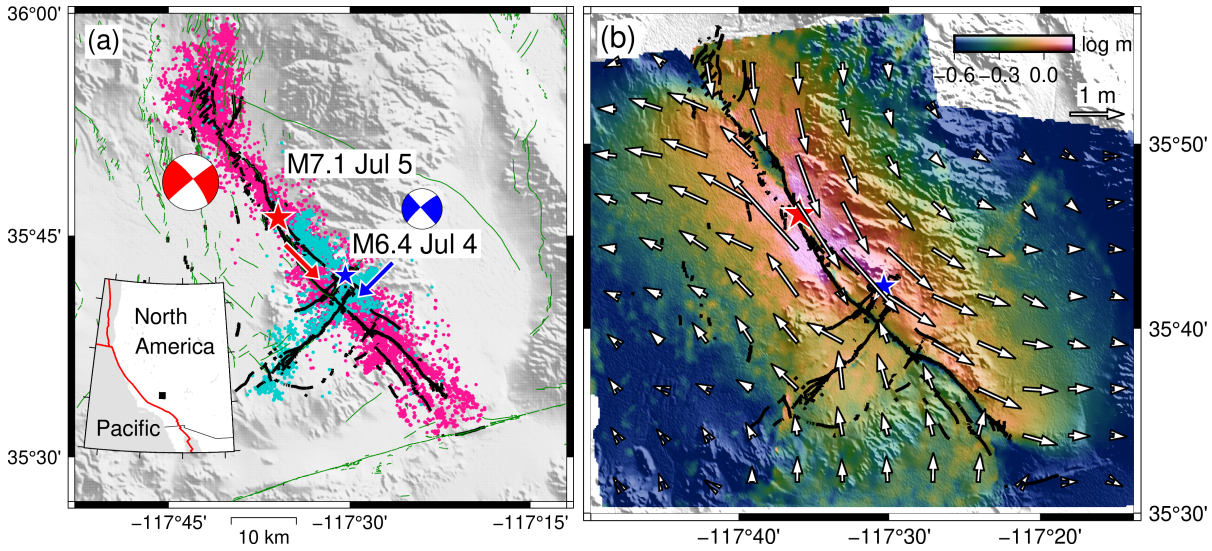



Figure 1: **Aftershocks and coseismic surface displacements due to the 2019 Ridgecrest earthquakes.** (a) Map of the epicentral area. Black wavy lines denote surface offsets due to the Ridgecrest earthquakes mapped by field surveys[30]. Red and blue stars denote the epicenters of the M7.1 and M6.4 earthquakes, and red and blue "beach balls" and arrows denote the focal mechanisms and the average fault strikes, respectively. Teal and magenta dots denote the aftershocks of the M6.4 and M7.1 events, respectively[26]. Thin green lines denote mapped active faults[31]. The inset shows the site location (black rectangle) with respect to the plate boundary (red line). (b) Coseismic displacements derived from space geodetic data (see Methods). Color denotes the logarithm (base 10) of the amplitude of horizontal displacement[32], in meters ($10^{-0.6} \approx 0.25$m, $10^{-0.3} \approx 0.5$m), and arrows denote the displacement vectors on a sub-sampled grid. Vertical displacements are shown in Supplementary Fig. 1.

seismicity[33]. The principal compression and shortening axes are in general agreement, except in areas with sparse seismicity and/or PBO station coverage (e.g., in the SW corner of Fig. 2). Around the epicenter of the $M_w$7.1 mainshock, the orientations of $\sigma_{Hmax}$ and $\dot{\varepsilon}_{Hmax}$ are essentially north-south, with the contraction rate axis possibly oriented slightly more easterly compared to the compression axis. Within the uncertainties, the $\sigma_{Hmax}$ and $\dot{\varepsilon}_{Hmax}$ axes bisect an angle formed by the cross faults ruptured by the 2019 Ridgecrest earthquakes (Supplementary Fig. 2).

**Mechanisms responsible for development of cross-faults**

Previous studies suggested that the pattern of high-angle faulting observed during the 2019 sequence results from either near-zero coefficient of friction, so that the crustal strength is limited to cohesion, or rock failure due to dynamic stress perturbations near a propagating rupture front[26]. While the latter might be responsible for small-scale "wing" faults oriented at high angle with respect to the main rupture[35], it doesn't apply to the two largest events of the 2019 sequence that were separated by a day (Fig. 1a). Also, inspection of prior background seismicity reveals a number of lineated structures that closely follow the strike of the right- and left-lateral faults ruptured during the 2019 sequence[36]. Several of such lineations are marked by the red and blue dashed lines in Fig. 2. These observations indicate a widespread distribution of active cross-faults in the Ridgecrest area that cannot be attributed to the effects of dynamic off-fault yielding.

Another possible explanation for the nearly-orthogonal fault orientation is strain localization in the ductile lower crust[37,38]. If strength of the continental crust is dominated by a ductile substrate, development of ductile shear zones may dictate fault orientations in the upper brittle crust. Since the ductile rheology is essentially independent of the mean stress, shear zones are expected to align at 45 degrees with respect to the principal stress axes, thus forming a right angle between the conjugate shear zones. Several lines of arguments however suggest that this mechanism is unlikely responsible for the observed fault geometries in the Ridgecrest area. First, a potential for strain localization in the ductile regime is inversely proportional to the effective viscosity[39]. Localized shear zones are less likely to form in a warm stretched crust such as that in the Ridgecrest area, characterized by a recent volcanism and ongoing geothermal activity[40]. Second, ductile shear zones are unlikely to develop below immature low slip rate faults, especially small, broadly distributed, low offset faults such as those abundantly present in the Ridgecrest area (Fig. 2). Finally, even if multiple conjugate faults were associated with deep ductile roots, the respective network of intersecting ductile shear zones would not be able to preserve its geometry under finite strain.

It might be tempting to interpret ubiquitous high-angle faults in the Ridgecrest area, including the 2019 ruptures (Fig. 2), as well as their orientation with respect to the principal compressive stress (Supplementary Fig. 2), in terms of a low coefficient of friction in the upper crust. If the observed active faults represent failure on optimally oriented planes (i.e., $2\theta_o$ >75 degrees), the respective coefficient of friction is smaller than 0.3, well below the experimentally determined values for most rock types[3,23]. If so, this would have profound implications for the mechanics of faulting and strength of the brittle part of the lithosphere. Below we demonstrate that the angle between cross-faults involved in the Ridgecrest sequence is not an optimal angle for the Mohr-Coulomb failure, and that the brittle strength of the

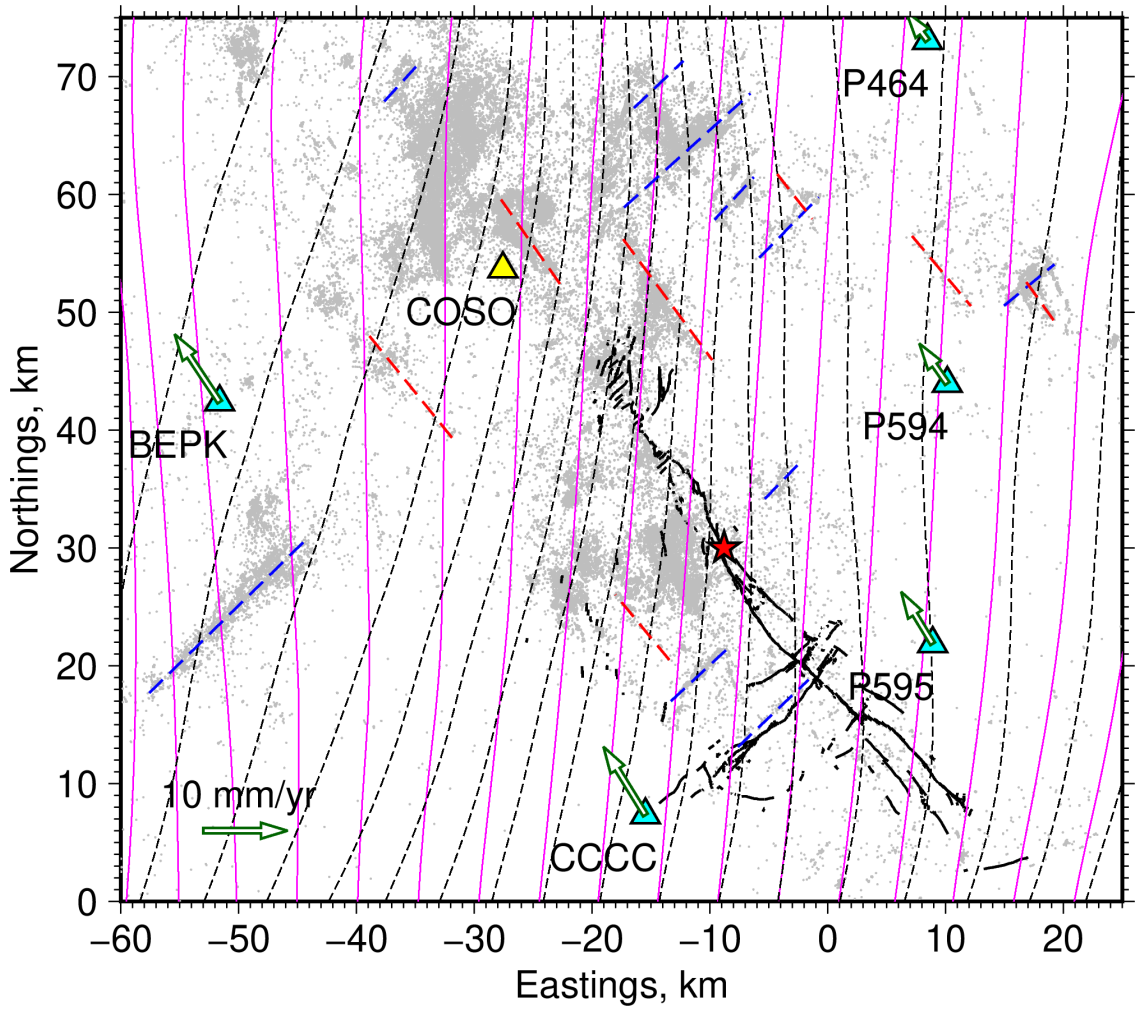



Figure 2: **Orientation of the principal stress and strain rate axes in the 2019 mainshock area.** Black dashed lines denote trajectories of the maximum horizontal compression ($\sigma_{Hmax}$)[33], magenta lines denote the direction of the maximum horizontal shortening rate ($\dot{\varepsilon}_{Hmax}$, see Methods), and grey dots denote the background seismicity (1981-June 2019)[34]. Filled triangles and green arrows denote the location of continuous GNSS sites and secular velocities (with respect to site SHOS, see Supplementary Fig. 3). Black solid lines denote surface traces of the 2019 Ridgecrest earthquakes. Blue and red dashed lines denote lineations in the background seismicity that are parallel to the left- and right-lateral faults involved in the 2019 $M_w$6.4 foreshock and the $M_w$7.1 mainshock (see Fig. 1). Local origin is at 117.5°W, 35.5°N.

seismogenic crust is in agreement with the Byerlee's law at the onset of faulting.

**Fault rotation from long-term tectonic deformation**

Theoretical considerations confirmed by observations suggest that tectonic deformation that promotes faulting, over time gives rise to a rotation of active faults away from the shortening axis[41,42]. The amount of rotation depends on the rate of deformation and the fault age. We use the modern deformation rates calculated using the Global Navigation Satellite System (GNSS) data (Supplementary Figs. 3-6) to estimate the time required to rotate conjugate faults from an initially optimal orientation ($2\theta_o \sim 50 - 60^\circ$) to the observed configuration ($2\theta \sim 75 - 90^\circ$, Supplementary Fig. 2). As a preliminary, we develop an analytic solution for the case of pure shear (see section "Fault rotation under pure shear" in Supplementary Information). The results are shown in Supplementary Fig. 7. Given the present-day shortening rate of $\sim 3 \cdot 10^{-2}$ Myr$^{-1}$ (Supplementary Fig. 5), optimally oriented faults are expected to rotate by 10-15 degrees over a time period on the order of 5-10 Myr (Supplementary Fig. 7). The resulting rotation is symmetric with respect to the shortening axis. The estimated age of rotation agrees well with time since the inception of the Eastern California Shear Zone (ECSZ)[43], suggesting that the currently active cross-faults (Figs. 1 and 2) may indeed have formed at optimal angles with respect to the compression axis at the early stages of initiation of the ECSZ, and subsequently rotated toward their current (non-optimal) orientations.

To further explore this possibility, we performed calculations in which we relaxed a number of simplifying assumptions. In particular, instead of the infinitesimal strain rate tensor, we used secular velocities measured with GNSS (Fig. 2 and Supplementary Fig. 4) to track rotation of linear markers that were initially optimally oriented with respect to the principal compression axis. The only assumptions behind this model are that (i) the present-day deformation is indicative of deformation over the last several million years, and (ii) the principal compression axis is the same as the principal shortening axis. Fig. 3a shows the predicted fault orientations (thin color lines) as a function of time, for the last 6 Myr. Also shown for reference are surface traces of the best-fit fault model of the 2019 Ridgecrest events [28]. While the relative rotation between left- and right-lateral conjugate faults predicted by the long-term tectonic deformation model is able to explain the observed angles between faults ruptured during the Ridgecrest sequence, as well as other active faults in the area (Fig. 2), the individual fault strikes predicted by the rotation model do not quite match the observed ones (Fig. 3a).

From Fig. 3a, one can notice that a better agreement can be rendered by a modest counter-clockwise rotation of the entire set of thin color lines. This is equivalent to suggesting that the orientation of the principal compression axis at the time of inception of the ECSZ was slightly different from its current orientation suggested by inversions of the earthquake focal mechanism data (Fig. 2). Fig. 3b presents a model in which new faults are formed at optimal angles (assuming a typical value of the coefficient of friction of 0.6) with respect to the $\sigma_{Hmax}$ axis oriented 5 degrees west of north. In this case, a good match between the predicted and observed fault geometries is obtained at 5 Myr after the fault initiation (purple lines in Fig. 3b). The inferred origin time is a function of the deformation history, but we note that values between 5 Myr ago (a constant strain rate) and 10 Myr ago (a linear increase from zero to the present-day strain rate) likely bracket a possible range of

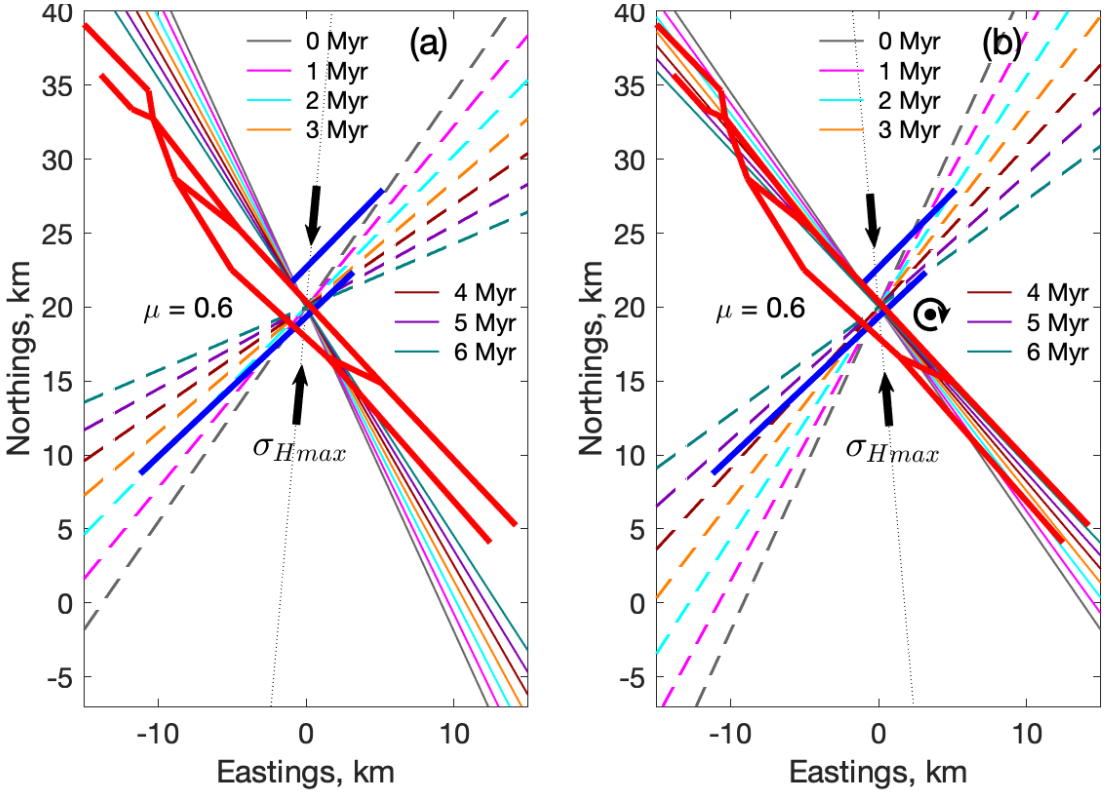



Figure 3: **Fault rotation predicted by extrapolation of the present-day velocity field into the geologic past.** (a) Orientations of right- and left-lateral faults (thin solid and dashed lines, respectively), as a function of time since their formation at an optimal angle with respect to the principal compression axis (assumed to be coincident with the present-day shortening rate axis). Thick red and blue lines denote surface traces of the right- and left-lateral faults from the best-fit slip model of the 2019 Ridgecrest earthquakes [28]. (b) Same as (a), except the maximum compression axis at the onset of faulting is oriented 5 deg. west of north.

deformation histories, and are in excellent agreement with geologic constraints (6-10 Myr) [43]. Sensitivity of model predictions to the assumed values of the coefficient of friction is evaluated in Supplementary Fig. 8.

Our analysis shows that the initial model assumptions were not strictly valid. Both the $\sigma_{Hmax}$ and $\dot{\varepsilon}_{Hmax}$ axes likely underwent a small clockwise rotation since the onset of faulting caused by reorganization of the plate boundary and formation of the ECSZ. Recall that in the epicentral area of the 2019 Ridgecrest earthquakes, the shortening rate axis is oriented more easterly compared to the compression axis (Fig. 2 and Supplementary Fig. 2). While the difference in orientations is likely within the data uncertainties, we note that for a non-stationary deformation scenario the axes of compression and instantaneous shortening do not need to coincide.

## Geologic evidence of finite strain

Results shown in Fig. 3 suggest that the fault rotation model is a reasonable explanation for the observed fault geometry. However they alone do not rule out an alternative hypothesis, namely that the currently active cross-faults are optimally oriented for failure. The key discriminant between the two interpretations is the fault age. While it may be difficult to constrain the total offset for all of the linear features expressed in microseismicity (Fig. 2), there is geologic evidence indicating that cross-faults that broke the Earth's surface have accommodated finite strain commensurate with the total amount of shear since the inception of the ECSZ. Fig. 4 shows a satellite photo of an outcrop at the eastern end of the NE-striking left-lateral fault system ruptured by the $M_w$6.4 foreshock. The outcrop features several igneous dikes that have the same trend as the Independence dike swarm, an extensive dike swarm in Eastern California emplaced around 150 Myr ago[44]. The exposed dikes are offset by left-lateral faults that have the same trend as the NE-striking cross-faults ruptured in 2019 (Fig. 4 and Supplementary Fig. 9), and some of the faults that cut the dikes were indeed activated by 2019 earthquakes (e.g., Supplementary Fig. 9a). The apparent average spacing between the faults of ∼150-200 m, and the average offsets on the order of a few tens of meters (Fig. 4) indicate that the faults have accommodated shear strain on the order of 10%. This is comparable to the total shear strain produced by integrating the present-day deformation field (Fig. 2 and Supplementary Fig. 6) over the life time of the ECSZ (i.e., several Myr). Additional geologic and geomorphologic evidence also exist regarding longevity of the right-lateral fault system[30]. These arguments lend further support to the hypothesis that the abundant cross-faults identified in the Ridgecrest area formed at the early stages of the ECSZ at optimal angles with respect to the principal compression axis, remained active over the last several millions of years, and were gradually rotated to their current configuration by the long-term tectonic motion.

A notable feature of fault rotation predicted by models shown in Fig. 3 is a pronounced asymmetry between the right- and left-lateral fault systems. Right-lateral faults essentially preserve their orientation throughout geologic time, while left-lateral faults accommodate most of the rotation. This is a well-recognized but poorly understood feature of deformation in the ECSZ[12]. In case of pure shear, the two sets of conjugate faults are expected to rotate symmetrically with respect to the shortening axis. Ron et al.[12] proposed that the observed asymmetry is caused by a large (20-25°) rotation of the principal stress axis coeval with faultling. Our model naturally explains the asymmetry due to the fact that deformation in the ECSZ is closer to simple shear rather than pure shear (Fig. 2). Because simple shear intrinsically involves rotation[45], the latter combines destructively with rotation due to axial shortening in case of right-lateral faults, and constructively in case of left-lateral faults, producing the observed asymmetry (Fig. 3). This may also explain why right-lateral faults grow into connected structures that ultimately dominate the seismic moment release in the ECSZ, while left-lateral faults tend to be disrupted and disorganized as they rotate away from the favorable orientation. An eventual de-activation of left-lateral faults may be delayed by the onset of enhanced weakening (either static or dynamic). Conditions for the onset of enhanced weakening are poorly understood, but are likely related to shear localization and structural maturity of fault zones, evolution of porosity, mineral alteration, etc. Persistence of slip on faults that formed at optimal angles and are now at $\sim 45^\circ$ to the principal stress

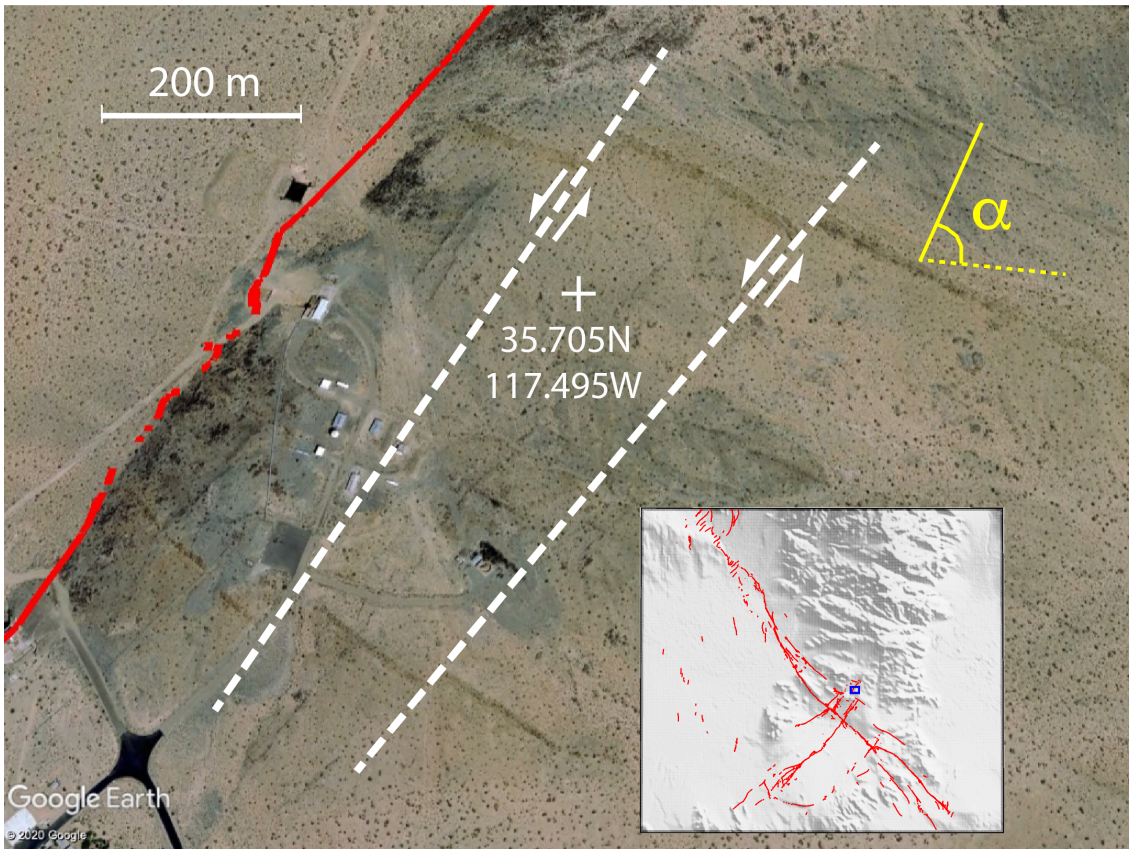



Figure 4: **Finite strain and rotation recorded by offset dikes.** Satellite photo of a dike swarm offset by left-lateral faults (white dashed lines) that have the same attitude as the 2019 left-lateral rupture that produced the M6.4 foreshock (red line). $\alpha$ is the angle between the axes of the least compressive stress acting at present (dashed yellow line) and at the time of dike emplacement (solid yellow line). White cross marks the indicated coordinates. The inset shows the outcrop location (blue rectangle) with respect to the entire earthquake rupture (red lines). Photo is from Google Earth.

axis (Fig. 2) suggests some form of enhanced weakening, in particular because the rotated faults co-exist with (presumably younger) faults that are more optimally oriented for failure. We note that the 2019 $M_w$7.1 mainshock nucleated on one of such more optimally oriented faults, and proceeded to rupture a pre-existing less favorably oriented fault, suggestive of dynamic weakening[28].

Our preferred model (Fig. 3b) is not sensitive to the time history of rotation of the principal stress axes. However, we note that orientation of dikes of the Independence dike swarm (Fig. 4 and Supplementary Fig. 9) is consistent with the sense of rotation inferred from our analysis (Fig. 3b). Given that a normal to a dike plane marks the paleo-axis of the least compressive stress[46], the angle between the axis of the present-day least compressive stress (orthogonal to the axis of $\sigma_{Hmax}$, see Fig. 2) and the least compressive stress acting at the time of dike intrusion is $\alpha \sim 60 - 70°$ (Fig. 4 and Supplementary Fig. 9). Dividing $\alpha$ by the dike age of $\sim$ 150 Myr[44] yields an apparent rotation rate of the principal stress axes on the order of 0.4-0.5°/Myr, a factor of 2 to 5 smaller than the average rotation rate of $\sigma_{Hmax}$ over the last 5-10 Myr (1-2°/Myr, Fig. 3b). The former rate is an upper bound because some fraction of $\alpha$ is likely due to axial shortening, rather than the absolute rotation of the principal stress axes. It follows that the clock-wise rotation of the principal stress axes was occurring well before the initiation of the ECSZ, but substantially accelerated over the last 5-10 Myr.

A kinematic model of the origin of cross-faults proposed in this study links the present-day fault geometry to the deformation history and age of the ECSZ constrained by geodetic and geologic observations, respectively. It may also be applicable to other areas of high-angle strike-slip conjugate faulting[2,47], as well as the observed clustering of the dip angles of normal earthquakes in the continental[42] and oceanic[22] lithosphere.

## Methods

The horizontal coseismic surface displacements shown in Fig. 1b were computed by inverting Synthetic Aperture Radar (SAR) data that represent diverse projections of the surface displacement field[48,49], including line of sight displacements (Sentinel-1A/B and ALOS-2 interferograms), range offsets (Sentinel-1A/B), and azimuth offsets (Cosmo-Skymed), from ascending and descending satellite tracks. The input data are from ref.[28] (also see section "Online data" in Supplementary Information). To reduce speckle, the offset maps were filtered using a 1km Gaussian filter. For each pixel we formed a system of linear equations by adding the respective unit look vectors as rows to the design matrix, and the observed quantity to the data vector. The system was inverted to obtain the 3 orthogonal components of the displacement vector subject to two conditions: (i) more than two observations from different data sets are available for a given pixel, and (ii) a condition number of the design matrix is less than some threshold (150 in our calculations). The first condition ensures that the system is not under-determined, and the second condition ensures that there is a sufficient diversity in the look angles (i.e., the solution is not highly unstable with respect to the data errors).

To analyze secular deformation in the Ridgecrest area, we used data from the continuously recording GNSS sites of PBO within $\sim$200 km from the 2019 mainshock (Supplementary Fig. 3). We used solutions for daily positions provided by UNAVCO. The data were

screened using the following criteria: (i) the site must have been in operation for the last 15 years (since 2004, to minimize transients from the 1992 Landers and the 1999 Hector Mine earthquakes[39]), and (ii) over the respective time period, the fraction of missing data is less than 30%. After the initial quality checking of the data, we have eliminated sites for which the displacement time series exhibited a strong non-linear behavior (e.g. site HIVI). We also excluded site COSO, which secular velocities are affected by production at the nearby geothermal plant[40,50]. Sites that were used in the analysis of secular deformation are shown as blue triangles in Supplementary Fig. 3. To compute secular velocities, we first cleaned up the UNAVCO timeseries by removing outliers and offsets (Supplementary Fig. 4). We then fitted a linear function to the cleaned timeseries for each component of the displacement vector. The slope of the best-fit line represents a respective component (i.e., E or N) of the secular velocity vector. We verified the robustness of the derived velocity field by predicting the secular velocity at site TOWG that is closest to the mainshock epicenter (see Supplementary Fig. 3), but was excluded from the analysis because it was installed only 5 years ago. The interpolated secular velocities show a good agreement with the observed time series at site TOWG (Supplementary Fig. 5), indicating that the derived velocity field is accurate and has a predictive power at spatial scales that are less than the distance between the continuous GNSS sites used in the analysis.

To compute the strain rate and rotation rate tensors from secular velocities, we used Delaunay triangulation to identify the nearest GNSS sites (Supplementary Fig. 6). For each triplet of sites forming vertices of the Delaunay triangles, we subtracted velocity of one site from the velocities of the remaining two sites. Assuming that the strain rate and the rotation rate are constant within a triangle, this gives rise to a system of 4 linear equations with 4 unknowns, $v_i = \dot{\varepsilon}_{ij} x_j + \omega_{ij} x_j$, where $i = E, N$ are the components along the respective coordinate axis, $\dot{\varepsilon}_{ij}$ is the 2-D strain rate tensor, $\omega_{ij}$ is the rotation rate tensor (anti-symmetric with zero diagonal components), $x_j$ is the baseline vector from the reference site, and summation is implied over repeating indices. After obtaining components of the strain rate tensor at each resolution cell, we computed the magnitude and orientation of the principal shortening rate as follows: $\dot{\varepsilon}_{Hmax} = 0.5(\dot{\varepsilon}_{EE} + \dot{\varepsilon}_{NN} - [(\dot{\varepsilon}_{EE} + \dot{\varepsilon}_{NN})^2 + \dot{\varepsilon}_{EN}^2]^{1/2})$, $\phi = 0.5(\arctan[\dot{\varepsilon}_{EN}/(\dot{\varepsilon}_{EE} - \dot{\varepsilon}_{NN})] + \pi)$ (see Supplementary Fig. 6).

## Data availability

All data used in this study are open access, available at:

First motion focal mechanism of the 2019 M7.1 mainshock:
`https://earthquake.usgs.gov/earthquakes/eventpage/ci38457511/focal-mechanism`,
last accessed May 2020.

Seismic moment of the 2019 M7.1 mainshock:
`https://earthquake.usgs.gov/earthquakes/eventpage/ci38457511/moment-tensor`, last accessed May 2020.

Seismic moment of the 2019 M6.4 foreshock:

https://earthquake.usgs.gov/earthquakes/eventpage/ci38443183/moment-tensor, last accessed May 2020.

Waveform-relocated earthquake catalog for Southern California[34]: https://scedc.caltech.edu/research-tools/alt-2011-dd-hauksson-yang-shearer.html, last accessed May 2020.

GNSS position time series from the Plate Boundary Observatory: DOI:10.7283/P2HT0Z https://www.unavco.org/data/gps-gnss/gps-gnss.html, last accessed May 2020.

Coseismic displacement data and fault slip models[28]: DOI:10.5281/zenodo.4646321

### Code availability

Matlab codes used to generate results presented in this study are available at: DOI:10.5281/zenodo.4646292

## References


[1] Anderson, E. M. *The dynamics of faulting* (206 pp., Oliver and Boyd, Edinburgh, 1951).

[2] Scholz, C. H. *The mechanics of earthquakes and faulting* (3rd Ed., 493 pp., Cambidge Univ. Press, New York, NY, 2019).

[3] Byerlee, J. Friction of rock. *Pure Appl. Geophys.* **116**, 615–626 (1978).

[4] Sibson, R. H. Rupture nucleation on unfavorably oriented faults. *Bull. Seism. Soc. Am.* **80**, 1580–1604 (1990).

[5] Lockner, D. A., Byerlee, J., Kuksenko, V., Ponomarev, A. & Sidorin, A. Observations of quasistatic fault growth from acoustic emissions. In Evans, B. & Wong, T. (eds.) *Fault mechanics and transport properties of rocks*, 3–31 (Academic, San Diego, CA, USA, 1992).

[6] Walsh, J. & Watterson, J. Dips of normal faults in British Coal Measures and other sedimentary sequences. *Journal of the Geological Society* **145**, 859–873 (1988).

[7] Collettini, C. & Sibson, R. H. Normal faults, normal friction? *Geology* **29**, 927–930 (2001).

[8] Mount, V. & Suppe, J. State of stress near the San Andreas fault: Implications for wrench tectonics. *Geology* **15**, 1143–1146 (1987).

[9] Zoback, M. D. *et al.* New evidence on the state of stress of the San Andreas fault system. *Science* **238**, 1105–1111 (1987).

[10] Wernicke, B. Low-angle normal faults and seismicity: A review. *J. Geophys. Res.* **100**, 20159–20174 (1995).

[11] Wang, K. & Fialko, Y. Observations and modeling of co- and postseismic deformation due to the 2015 $M_w$ 7.8 Gorkha (Nepal) earthquake. *J. Geophys. Res.* **123**, 761–779 (2018).

[12] Ron, H., Beroza, G. & Nur, A. Simple model explains complex faulting. *Eos, Transactions American Geophysical Union* **82**, 125–129 (2001).

[13] Sibson, R. Reverse fault rupturing: competition between non-optimal and optimal fault orientations. *Geological Society, London, Special Publications* **367**, 39–50 (2012).

[14] Wintsch, R., Christoffersen, R. & Kronenberg, A. Fluid-rock reaction weakening of fault zones. *J. Geophys. Res.* **100**, 13021–13032 (1995).

[15] Faulkner, D. R., Mitchell, T. M., Healy, D. & Heap, M. J. Slip on 'weak' faults by the rotation of regional stress in the fracture damage zone. *Nature* **444**, 922–925 (2007).

[16] Noda, H., Dunham, E. & Rice, J. R. Earthquake ruptures with thermal weakening and the operation of major faults at low overall stress levels. *J. Geophys. Res.* **114**, B07302 (2009).

[17] Di Toro, G. *et al.* Fault lubrication during earthquakes. *Nature* **471**, 494–498 (2011).

[18] Han, R., Hirose, T. & Shimamoto, T. Strong velocity weakening and powder lubrication of simulated carbonate faults at seismic slip rates. *J. Geophys. Res.* **115** (2010).

[19] Brown, K. M. & Fialko, Y. "Melt welt" mechanism of extreme weakening of gabbro at seismic slip rates. *Nature* **488**, 638–641 (2012).

[20] Fialko, Y. Fracture and Frictional Mechanics - Theory. In Schubert, G. (ed.) *Treatise on Geophysics, 2nd. Ed., Vol. 4*, 73–91 (Elsevier Ltd., Oxford, 2015).

[21] Chester, J. S., Chester, F. M. & Kronenberg, A. K. Fracture surface energy of the Punchbowl fault, San Andreas system. *Nature* **437**, 133–136 (2005).

[22] Copley, A. The strength of earthquake-generating faults. *Journal of the Geological Society* **175**, 1–12 (2018).

[23] Mitchell, E., Fialko, Y. & Brown, K. M. Velocity-weakening behavior of Westerly granite at temperature up to 600° C. *J. Geophys. Res.* **121**, 6932–6946 (2016).

[24] Angelier, J. Tectonic analysis of fault slip data sets. *J. Geophys. Res.* **89**, 5835–5848 (1984).

[25] Nicholson, C., Seeber, L., Williams, P. & Sykes, L. R. Seismic evidence for conjugate slip and block rotation within the San Andreas fault system, southern California. *Tectonics* **5**, 629–648 (1986).

[26] Ross, Z. E. *et al.* Hierarchical interlocked orthogonal faulting in the 2019 Ridgecrest earthquake sequence. *Science* **366**, 346–351 (2019).

[27] Chen, K. *et al.* Cascading and pulse-like ruptures during the 2019 Ridgecrest earthquakes in the Eastern California Shear Zone. *Nature Communications* **11**, 1–8 (2020).

[28] Jin, Z. & Fialko, Y. Finite slip models of the 2019 Ridgecrest earthquake sequence constrained by space geodetic data and aftershock locations. *Bull. Seism. Soc. Am.* **110**, 1660–1679 (2020).

[29] Magen, Y., Ziv, A., Inbal, A., Baer, G. & Hollingsworth, J. Fault rerupture during the July 2019 Ridgecrest earthquake pair from joint slip inversion of InSAR, optical Imagery, and GPS. *Bull. Seism. Soc. Am.* (2020).

[30] Ponti, D. *et al.* Documentation of surface fault rupture and ground deformation features produced by the Ridgecrest M6. 4 and M7. 1 earthquake sequence of July 4 and 5, 2019 (2020). In press.

[31] Jennings, C. & Bryant, W. Fault Activity Map of California (2010). California Division of Mines and Geology, Geologic Data Map No. 6.

[32] Fialko, Y. Probing the mechanical properties of seismically active crust with space geodesy: Study of the co-seismic deformation due to the 1992 $M_w$7.3 Landers (southern California) earthquake. *J. Geophys. Res.* **109**, B03307, 10.1029/2003JB002756 (2004).

[33] Yang, W. & Hauksson, E. The tectonic crustal stress field and style of faulting along the Pacific North America Plate boundary in Southern California. *Geophys. J. Int.* **194**, 100–117 (2013).

[34] Hauksson, E., Yang, W. & Shearer, P. M. Waveform relocated earthquake catalog for Southern California (1981 to 2011). *Bull. Seism. Soc. Am.* **102**, 2239–2244 (2012).

[35] Templeton, E. L. & Rice, J. R. Off-fault plasticity and earthquake rupture dynamics: 1. Dry materials or neglect of fluid pressure changes. *J. Geophys. Res.* **113** (2008).

[36] Fialko, Y. Estimation of absolute stress in the hypocentral region of the 2019 Ridgecrest, California, earthquakes. *J. Geophys. Res.* (submitted, 2021).

[37] Takeuchi, C. & Fialko, Y. Dynamic models of interseismic deformation and stress transfer from plate motion to continental transform faults. *J. Geophys. Res.* **117**, B05403, doi:10.1029/2011JB009056 (2012).

[38] Montesi, L. Fabric development as the key for forming ductile shear zones and enabling plate tectonics. *J. Struct. Geol.* **50**, 254–266 (2013).

[39] Takeuchi, C. & Fialko, Y. On the effects of thermally weakened ductile shear zones on postseismic deformation. *J. Geophys. Res.* **118**, 6295–6310 (2013).

[40] Fialko, Y. & Simons, M. Deformation and seismicity in the Coso geothermal area, Inyo County, California: Observations and modeling using satellite radar interferometry. *J. Geophys. Res.* **105**, 21781–21793 (2000).

[41] Nur, A., Ron, H. & Scotti, O. Fault mechanics and the kinematics of block rotations. *Geology* **14**, 746–749 (1986).

[42] Thatcher, W. & Hill, D. P. Fault orientations in extensional and conjugate strike-slip environments and their implications. *Geology* **19**, 1116–1120 (1991).

[43] Dokka, R. K. & Travis, C. J. Role of the Eastern California shear zone in accommodating Pacific-North American plate motion. *Geophys. Res. Lett.* **17**, 1323–1327 (1990).

[44] Chen, J. H. & Moore, J. G. Late Jurassic Independence dike swarm in eastern California. *Geology* **7**, 129–133 (1979).

[45] Savage, J., Gan, W. & Svarc, J. Strain accumulation and rotation in the Eastern California Shear Zone. *J. Geophys. Res.* **106**, 21995–22007 (2001).

[46] Fialko, Y. A. & Rubin, A. M. Thermal and mechanical aspects of magma emplacement in giant dike swarms. *J. Geophys. Res.* **104**, 23033–23049 (1999).

[47] Hudnut, K. W., Seeber, L. & Pacheco, J. Cross-fault triggering in the November 1987 Superstition Hills earthquake sequence, Southern California. *Geophys. Res. Lett.* **16**, 199–202 (1989).

[48] Fialko, Y., Simons, M. & Agnew, D. The complete (3-D) surface displacement field in the epicentral area of the 1999 $M_w$7.1 Hector Mine earthquake, southern California, from space geodetic observations. *Geophys. Res. Lett.* **28**, 3063–3066 (2001).

[49] Fialko, Y., Sandwell, D., Simons, M. & Rosen, P. Three-dimensional deformation caused by the Bam, Iran, earthquake and the origin of shallow slip deficit. *Nature* **435**, 295–299 (2005).

[50] Tymofyeyeva, E. & Fialko, Y. Mitigation of atmospheric phase delays in InSAR data, with application to the Eastern California Shear Zone. *J. Geophys. Res.* **120**, 5952–5963 (2015).

[51] Wessel, P., Smith, W. H. F., Scharroo, R., Luis, J. & Wobbe, F. Generic Mapping Tools: Improved Version Released. *Eos, Trans. AGU* **94**, 409–410 (2013).

Correspondence and requests for materials should be addressed to YF, yfialko@ucsd.edu

**Acknowledgments.** We thank O. Zielke and M.-H. Huang for their comments. This study was supported by NSF (grants EAR-1841273 and EAR-1945760) and NASA (grant 80NSSC18K0466). Figures were produced using Generic Mapping Tools (GMT)[51] and Matlab. The authors declare no competing interests.

**Author Contributions.** YF performed the data analysis and wrote the manuscript. ZJ provided a finite fault model of the 2019 Ridgecrest earthquakes, and contributed to the graphics design.

nature portfolio

https://doi.org/10.1038/s41561-021-00758-5

## Supplementary information

# Simple shear origin of the cross-faults ruptured in the 2019 Ridgecrest earthquake sequence

In the format provided by the authors and unedited

# Supplementary Information

## Simple shear origin of the cross-faults ruptured in the 2019 Ridgecrest earthquake sequence

Yuri Fialko and Zeyu Jin

**Contents**


| | |
|---|---|
| Evaluating the attitude of the 2019 ruptures | p. 2 |
| Fault rotation under pure shear | p. 3 |
| References | p. 4 |
| Supplementary Figure 1 | p. 6 |
| Supplementary Figure 2 | p. 7 |
| Supplementary Figure 3 | p. 8 |
| Supplementary Figure 4 | p. 9 |
| Supplementary Figure 5 | p. 10 |
| Supplementary Figure 6 | p. 11 |
| Supplementary Figure 7 | p. 12 |
| Supplementary Figure 8 | p. 13 |
| Supplementary Figure 9 | p. 14 |

## Evaluating the attitude of the 2019 ruptures

We quantified strike angles of the right- and left-lateral faults ruptured during the 2019 Ridgecrest sequence using several independent data sets. Centroid Moment Tensor (CMT) solutions are point-source approximations of finite ruptures that represent average rupture characteristics[1]. We used CMT solutions for the M6.4 foreshock and the M7.1 mainshock from the Global CMT catalog[2]. The latter provides both the components of the moment tensor, and the strike, dip and rake angles for the two nodal planes derived from the moment tensor. Estimated errors are provided only for components of the moment tensor. To evaluate the associated uncertainties in fault strike, we have randomly perturbed each component of the moment tensor by $3\sigma$, where $\sigma$ is the reported error for the respective component. The perturbed moment tensor was used to calculate strike angles for the main and auxiliary nodal planes. Calculations were repeated $10^4$ times. The maximum deviation from the CMT catalog value of the fault strike angle did not exceed 1 degree. The fault strikes suggested by the CMT solutions are shown as dashed lines in Supplementary Fig. 2.

Aftershocks provide another constraint on the rupture geometry, as they typically occur on or close to the rupture interface[3]. Estimating the fault strike however is not straightforward if more than one fault was activated during an earthquake, as was clearly the case in the 2019 Ridgecrest sequence (see Fig. 1 in the main text). In case of the M6.4 event that produced aftershocks on a set of NE and NW striking faults (Fig. 1a), we used a model employing mixture of two linear regressors based on the expectation-maximization (EM) algorithm[4]. The model estimates two linear trends in a scattered data set using trials with different random starting points, and is quite robust in case of noisy and multi-valued input data. For the M7.1 event, there is a well-defined dominant NW striking rupture (Fig. 1a), however a simple linear regression is hindered by aftershocks that are associated with multiple cross-faults[5]. In case of the mainshock, we use an unbiased linear regression[6,7] along with an iterative procedure to eliminate events that are further away than a prescribed distance $D$ from a current best-fitting linear trend. The cut-off distance $D$ is decreased from 7 to

3 km as a number of iterations increase. The strike angles suggested by the best-fit linear trends to the aftershock data are shown as dotted lines in Supplementary Fig. 2, along with the estimated uncertainties.

Finally, we collected statistics on the fault strike from a finite rupture model that incorporates data from field mapping of surface offsets, aftershock distribution at depth, and surface displacements away from the fault trace measured with space geodetic techniques[8]. Circular histogram plots in Supplementary Fig. 2 illustrate a distribution of fault strikes in the best-fit finite rupture model, scaled by the seismic moment released on faults of the respective orientation.

Also shown in Supplementary Fig. 2 are strike angles suggested by the first-motion focal mechanisms (thin solid lines; see Section "Online data"). While for the M6.4 foreshock the fault orientation suggested by the focal mechanism is in a good agreement with other estimates, in case of the M7.1 mainshock the fault strike suggested by the first-motion focal mechanism is notably different from fault strikes constrained by other data (Supplementary Fig. 2). This may be indicative of the rupture initiation on a plane that is more optimally oriented for failure with respect to the principal compression axis, and subsequent propagation on a pre-existing less favorably oriented fault[8]. Formal uncertainties on the orientation of nodal planes from the first-motion mechanism are fairly large (on the order of 10 degrees or more, mostly due to sensitivity of the inversion method to trade-offs between rupture strike, dip and rake)[9].

## Fault rotation under pure shear

Consider a case of homogeneous plane strain with eigenvalues $\varepsilon_i$ $(i = 1, 2)$ and eigenvectors that are aligned with the Cartesian coordinate axes $x_i$. We wish to find how the prescribed deformation changes the orientation of straight lines forming an angle $\pm\theta_o$ with respect to the $x_2$ axis. Because of the symmetry with respect to the $x_2$ axis, we only consider $x_2 > 0$. Prior to deformation, the line is defined by a diagonal of a surface element $\Delta x_i$, such that

$\theta_o = \arctan(\Delta x_2/\Delta x_1)$. After deformation, the sides of the surface element become $\Delta x_i + u_i$, where $u_i$ is a displacement of a point with initial coordinates $\Delta x_i$, $u_1 = \Delta x_1 \varepsilon_1$, $u_2 = \Delta x_2 \varepsilon_2$. In case of pure shear, $\varepsilon_1 = -\varepsilon_2 \equiv \varepsilon$. The element diagonal is rotated by an angle $\Delta\theta$,

$$\tan(\theta_o + \Delta\theta) = \frac{\Delta x_2 + u_2}{\Delta x_1 + u_1} = \tan\theta_o \frac{1-\varepsilon}{1+\varepsilon}. \tag{1}$$

Making use of the sum formula for tangent,

$$\tan(\theta_o + \Delta\theta) = \frac{\tan\theta_o + \tan\Delta\theta}{1 - \tan\theta_o \tan\Delta\theta}, \tag{2}$$

equation (1) gives rise to

$$\frac{1 + \frac{\tan\Delta\theta}{\tan\theta_o}}{1 - \tan\theta_o \tan\Delta\theta} = \frac{1-\varepsilon}{1+\varepsilon}. \tag{3}$$

Solving for $\Delta\theta$, we obtain

$$\Delta\theta = -\arctan\left[\frac{2\varepsilon \tan\theta_o}{1 + \varepsilon + (1-\varepsilon)\tan^2\theta_o}\right]. \tag{4}$$

Equation (4) can be used to evaluate rotation of an initially optimally oriented fault ($\theta_o = 0.5\arctan(\mu^{-1})$) as a function of time $t$, given $\dot{\varepsilon}_2 \equiv \dot{\varepsilon}_{Hmax}$, and $\varepsilon = \dot{\varepsilon}_{Hmax} t$. The resulting fault orientations $\theta(t) = \theta_o + \Delta\theta(t)$ are shown in Supplementary Fig. 7 for the observed value of $\dot{\varepsilon}_{Hmax}$ (Supplementary Fig. 6) and several assumed values of the coefficient of friction $\mu$.

# References


**1** Aki, K. & Richards, P. G. *Quantitative Seismology* (700 pp., Univ. Sci. Books, Sausalito, Calif., 2002).

**2** Ekström, G., Nettles, M. & Dziewoński, A. The global CMT project 2004–2010: Centroid-moment tensors for 13,017 earthquakes. *Physics of the Earth and Planetary Interiors* **200**, 1–9 (2012).

**3** Hauksson, E., Jones, L. M., Hutton, K. & Eberhart-Phillips, D. The 1992 Landers earthquake sequence: Seismological observations. *J. Geophys. Res.* **98**, 19835–19858 (1993).

**4** Dempster, A. P., Laird, N. M. & Rubin, D. B. Maximum likelihood from incomplete data via the EM algorithm. *Journal of the Royal Statistical Society: Series B (Methodological)* **39**, 1–22 (1977).

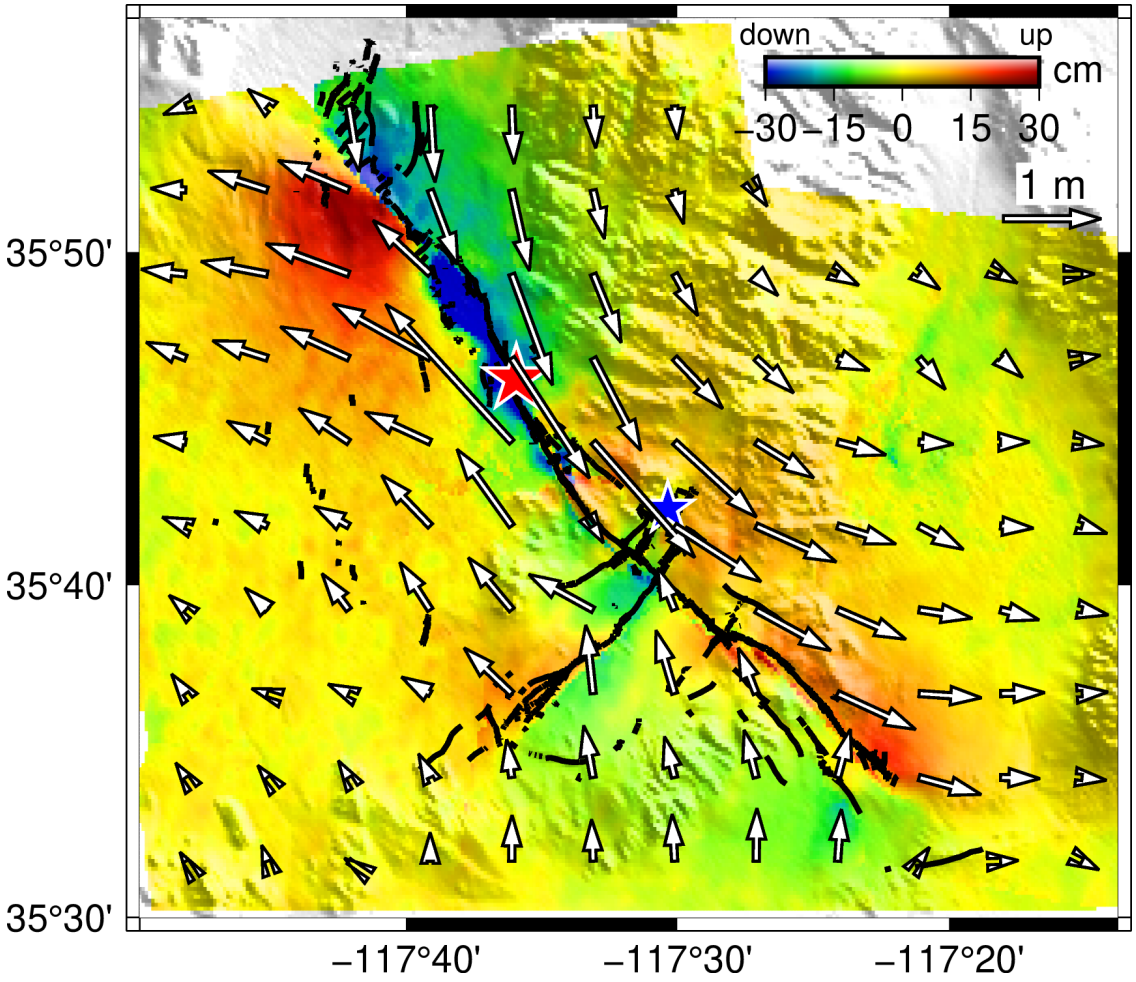
**5** Ross, Z. E. *et al.* Hierarchical interlocked orthogonal faulting in the 2019 Ridgecrest earthquake sequence. *Science* **366**, 346–351 (2019).

**6** Künsch, H. R., Stefanski, L. A. & Carroll, R. J. Conditionally unbiased bounded-influence estimation in general regression models, with applications to generalized linear models. *Journal of the American Statistical Association* **84**, 460–466 (1989).

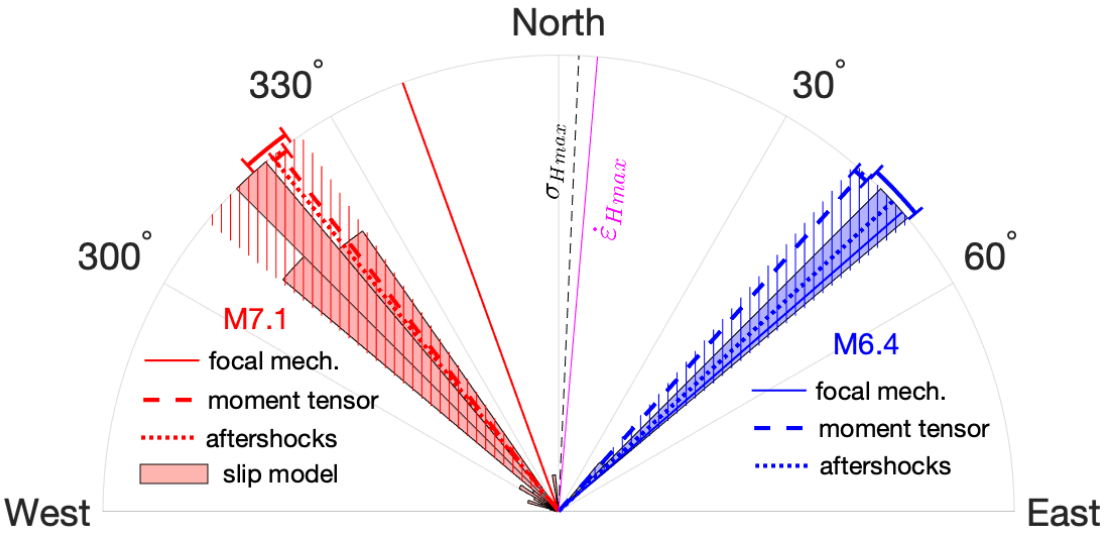
**7** Fialko, Y. Evidence of fluid-filled upper crust from observations of post-seismic deformation due to the 1992 $M_w$7.3 Landers earthquake. *J. Geophys. Res.* **109**, B08401, 10.1029/2004JB002985 (2004).

**8** Jin, Z. & Fialko, Y. Finite slip models of the 2019 Ridgecrest earthquake sequence constrained by space geodetic data and aftershock locations. *Bull. Seism. Soc. Am.* **110**, 1660–1679 (2020).

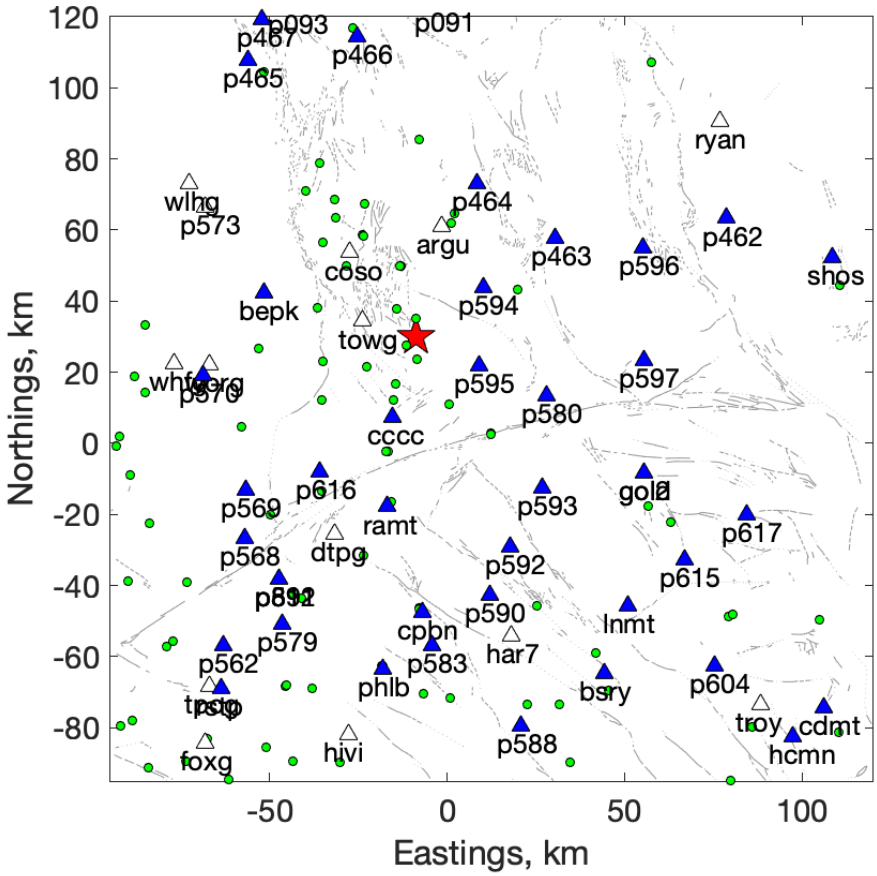
**9** Yang, W., Hauksson, E. & Shearer, P. M. Computing a large refined catalog of focal mechanisms for southern California (1981–2010): Temporal stability of the style of faulting. *Bull. Seism. Soc. Am.* **102**, 1179–1194 (2012).



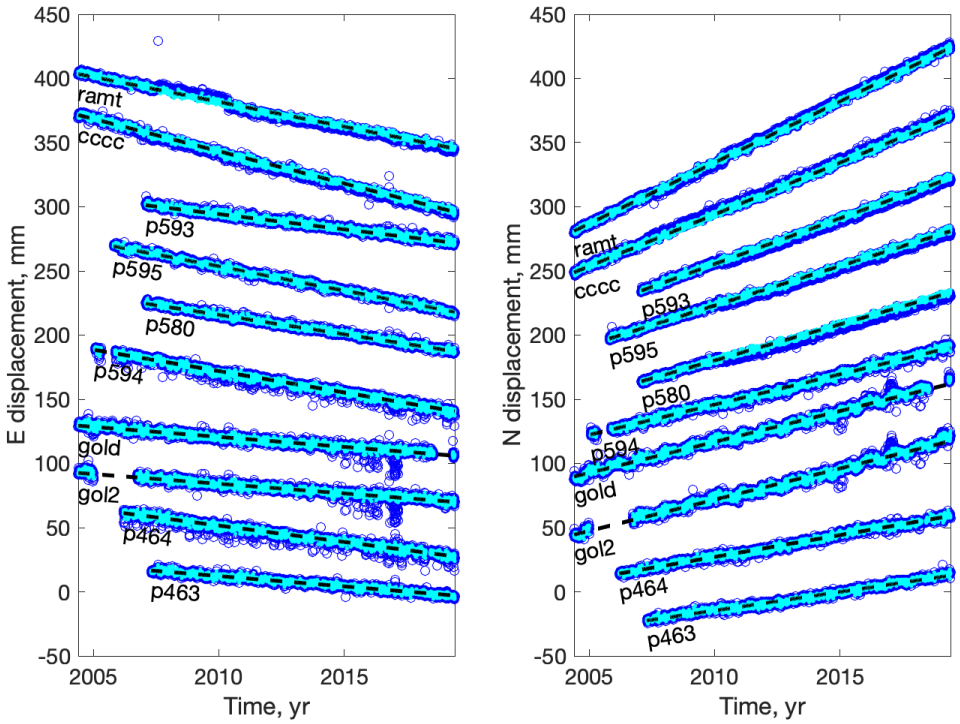

Supplementary Figure 1: A vertical component of the coseismic displacement field due to the July 2019 earthquakes. Note a color scale in centimeters. Other notation is the same as in Fig. 1b in the main text.



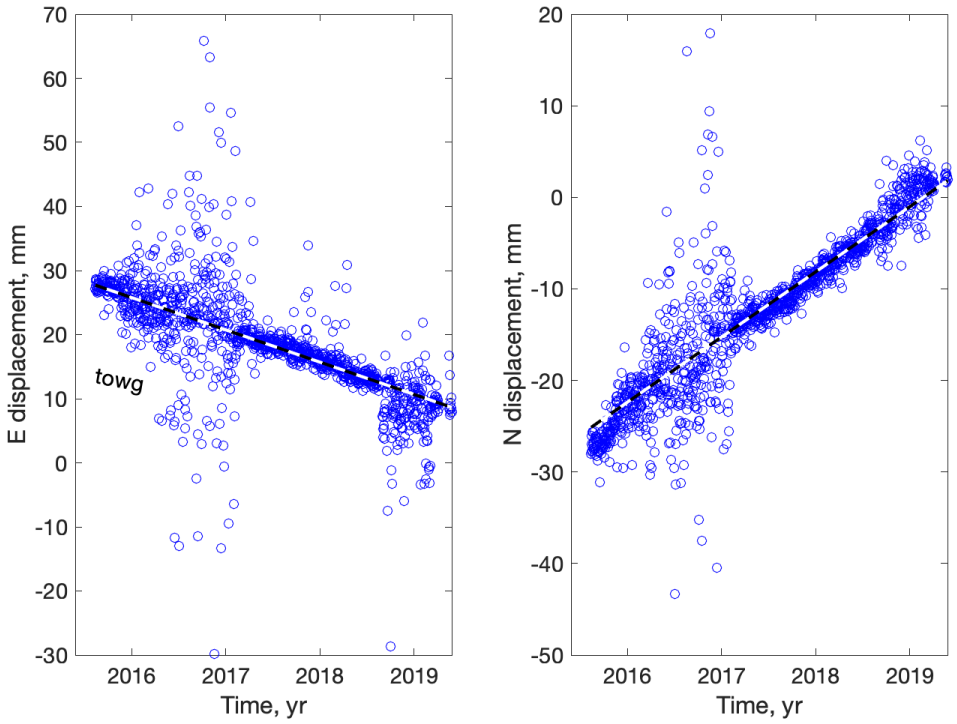

Supplementary Figure 2: Orientation of the left-lateral (blue color) and right-lateral (red color) faults ruptured by the M6.4 foreshock and the M7.1 mainshock, respectively. Different line styles denote fault strikes suggested by the first-motion focal mechanism, moment tensor, and linear fit to the aftershock epicenters. Rose diagrams denote fault strikes suggested by the best-fit slip model[8] (to save space, legend is shown for the right-lateral faults only). Length of the 5-degree bins is proportional to the seismic moment released by fault segments having the respective range of strikes. Hatched areas denote the admissible range of strike angles, including the uncertainties. Pink solid line and black dashed line denote orientations of the contraction rate and compression axes, respectively, around the epicenter of the M7.1 mainshock (see Fig. 2 in the main text).



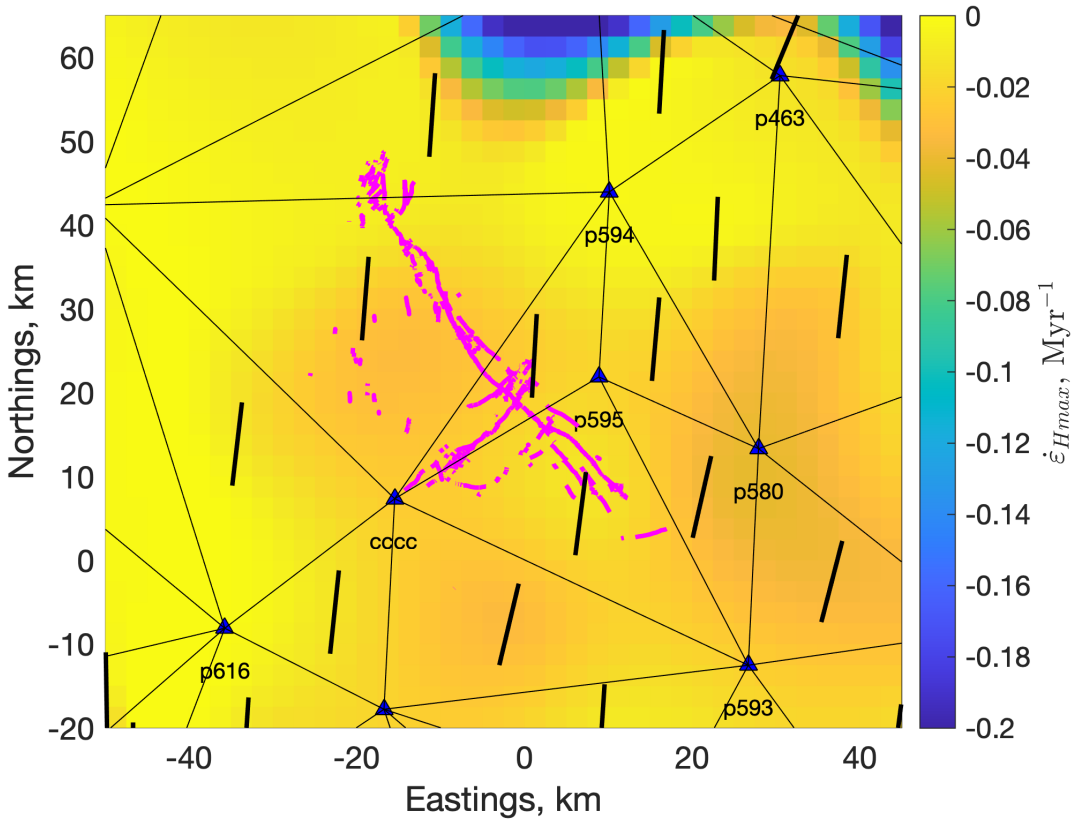

Supplementary Figure 3: Continuous GNSS (triangles) and seismic (green circles) stations within $\sim$ 100 km from the earthquake epicenter (red star). Blue triangles denote GNSS sites that satisfied the data selection criteria (see Methods section in the main text) and were used to compute the strain and rotation rate tensors.



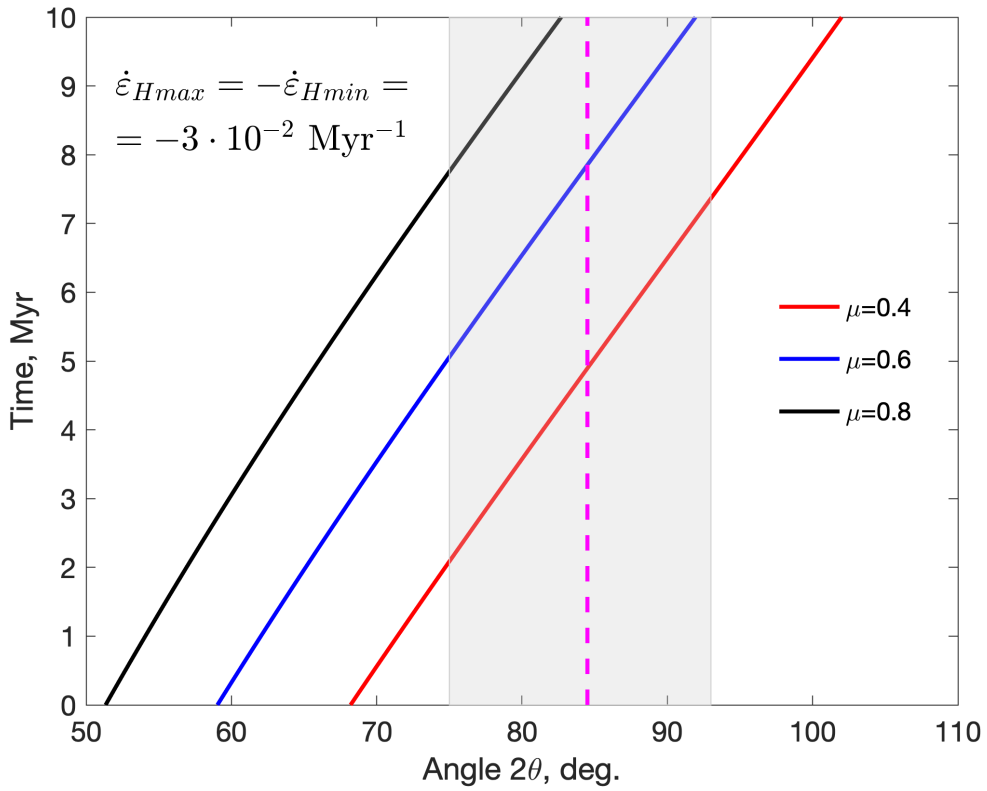

Supplementary Figure 4: Example timeseries of GNSS displacements from several continuous sites (see Supplementary Fig. 3). Blue circles: original solutions from UNAVCO. Cyan dots: data after removal of outliers and offsets. Dashed lines: best least-square fits to the cleaned data (cyan dots).



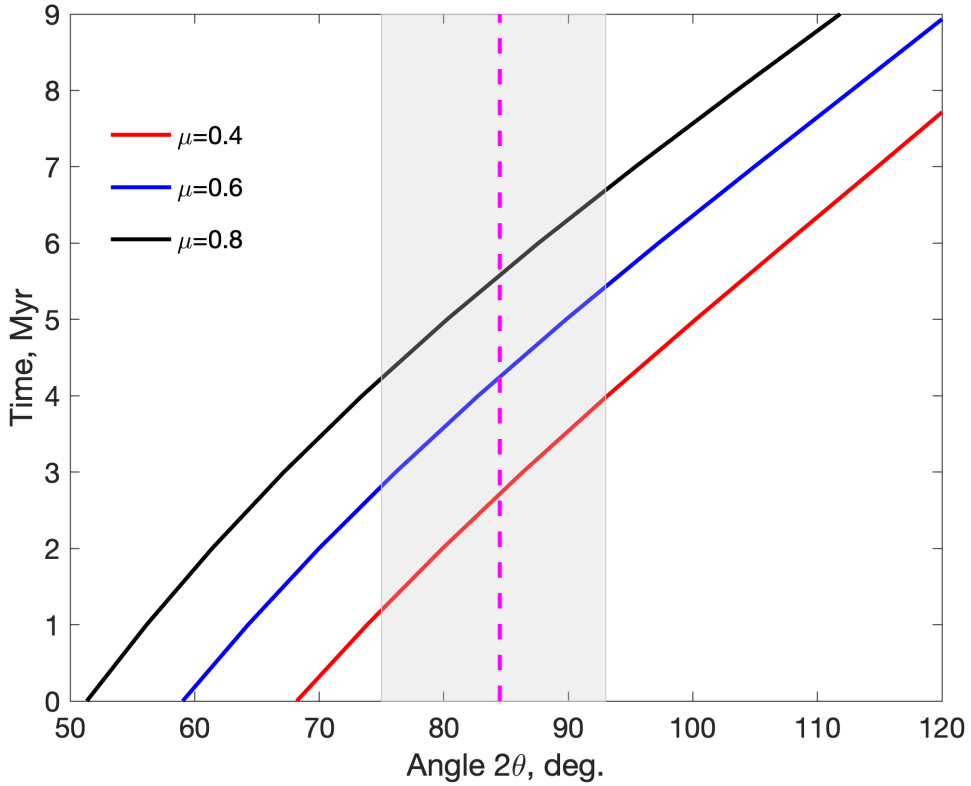

Supplementary Figure 5: A comparison of the horizontal velocity components obtained from interpolation of velocities from the selected sites (blue triangles in Supplementary Fig. 3) to the observed time series from site TOWG that was not included in the selection (blue circles; see site location in Supplementary Fig. 3). Black and white dashed lines denote predictions of the interpolation model.



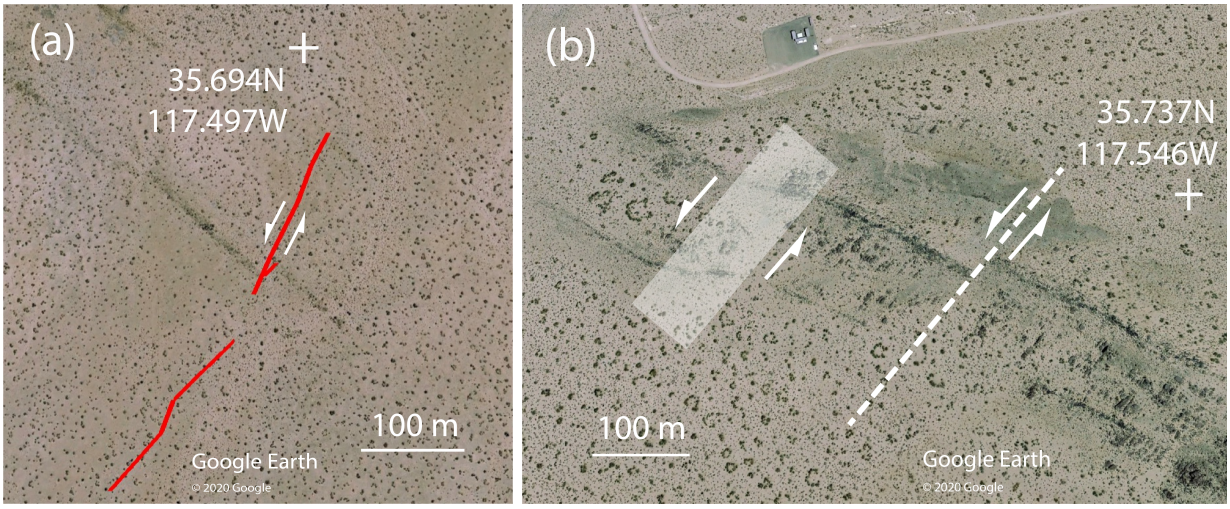

Supplementary Figure 6: The magnitude (color) and orientation (black tick marks) of the maximum horizontal shortening rate computed from the GNSS secular velocities. Magenta lines denote the surface trace of the 2019 earthquakes.




Supplementary Figure 7: Time required to produce a given angle between conjugate faults assuming a pure shear deformation at the observed present-day rate (equation 4 and Supplementary Fig. 6). Color lines correspond to the different assumed coefficients of friction. Grey area denotes the admissible range of angles between the left-and right-lateral faults of the Ridgecrest sequence (Supplementary Fig. 2). Dashed magenta line denotes the most likely value of $2\theta$.




Supplementary Figure 8: Same as Supplementary Fig. 7, calculated using finite displacements predicted by the present-day secular velocities over a given period of time.




Supplementary Figure 9: NW-trending igneous dikes offset by the NE-trending left-lateral faults. Notation is the same as in Fig. 4 in the main text. (a) A pre-existing left-lateral fault activated by the 2019 earthquakes. Red line denotes mapped coseismic offsets. (b) Examples of left-lateral dike offsets due to a localized fault (white dashed line) and a distributed shear zone (white shaded rectangle). Photos are from Google Earth.